JGR Space Physics

RESEARCH ARTICLE
10.1029/2025JA034503

An Explosive Leakage of Heavy Ions From Martian Crustal Magnetic Anomalies

Sanwei Cheng[1,2,3], Zhenpeng Su[1,2,3,4], Zewen Chen[1,2,3], Zhiyong Wu[1,2,3], Jing Wang[5], Zhonglei Gao[6], and Yuming Wang[1,2,3]

[1]National Key Laboratory of Deep Space Exploration, School of Earth and Space Sciences, University of Science and Technology of China, Hefei, China, [2]CAS Center for Excellence in Comparative Planetology, CAS Key Laboratory of Geospace Environment, Mengcheng National Geophysical Observatory, University of Science and Technology of China, Hefei, China, [3]Collaborative Innovation Center of Astronautical Science and Technology, Hefei, China, [4]State Key Laboratory of Lunar and Planetary Sciences, Macau University of Science and Technology, Macao, China, [5]Planetary Environmental and Astrobiological Research Laboratory (PEARL), School of Atmospheric Sciences, Sun Yatsen University, Zhuhai, China, [6]School of Physics and Electronic Sciences, Changsha University of Science and Technology, Changsha, China

Key Points:

- A transient suprathermal ion injection was observed to produce an ionospheric cold plasma depletion in a crustal magnetic anomaly
- Charge separation of reconnection jet created electrostatic potential enabling the escape of cold heavy ions
- Localized escape fluxes of heavy ions reached two orders of magnitude higher than background levels

Correspondence to:
Z. Su,
szpe@mail.ustc.edu.cn

Citation:
Cheng, S., Su, Z., Chen, Z., Wu, Z., Wang, J., Gao, Z., & Wang, Y. (2025). An explosive leakage of heavy ions from Martian crustal magnetic anomalies. *Journal of Geophysical Research: Space Physics*, *130*, e2025JA034503. https://doi.org/10.1029/2025JA034503

Received 29 JUL 2025
Accepted 25 AUG 2025

Abstract Atmospheric escape processes are crucial for shaping the long-term surface habitability of terrestrial planets. A key question is how planetary magnetic fields influence atmospheric escape. On present-day Mars, there are crustal magnetic anomalies predominantly in the southern hemisphere, whose impact on the escape of ionospheric heavy ions remains under debate. Based on MAVEN observations, we propose a new candidate mechanism to explain how ionospheric heavy ions can escape from regions with strong crustal magnetic anomalies. This mechanism is triggered by reconnection between draped interplanetary and crustal magnetic fields, forming magnetic cusps with open field lines and generating plasma jets that impact the crustal anomalies. Within these anomalies, ions and electrons exhibit distinct spatial and temporal behaviors, leading to charge separation and the formation of an electrostatic potential. This potential lifts cold, heavy ions from the ionosphere along open field lines to escape altitudes. The process occurs within minutes, producing localized escape fluxes up to two orders of magnitude higher than background levels. This explosive leakage pattern may hold significance for other unmagnetized or weakly magnetized planets where magnetospheric and ionospheric boundaries converge.

1. Introduction

A habitable terrestrial planet requires a sufficiently dense atmosphere to maintain stable climate conditions, protect against harmful radiations, and support the presence of liquid water and complex ecosystems (e.g., Gronoff et al., 2020; Lammer et al., 2009; Owen, 2019; Tian, 2015). Within the habitable zone of our solar system, Mars exemplifies the profound consequences of atmospheric loss. Over its 4.5-billion-year history, Mars is believed to have transformed from a warm and wet environment to the cold, dry world we observe today (Jakosky & Phillips, 2001). The ongoing atmospheric escape on present-day Mars involves both neutral and ionized gas components (C. Dong et al., 2018; Lundin et al., 2007). Neutral gases are predominantly lost through thermal escape (Jeans, 2009), photochemical escape (e.g., Cui et al., 2019; Fox & Hać, 2018), and sputtering (Curry et al., 2025; Gu et al., 2020; Luhmann et al., 1992). Ionized gases, in contrast, are primarily lost through ionospheric ion pickup (e.g., Luhmann & Kozyra, 1991; Luhmann & Schwingenschuh, 1990) and other acceleration and heating processes (e.g., Brain et al., 2015; Collinson et al., 2015, 2019; Y. Dong et al., 2015; Dubinin et al., 1993, 2017; Ergun et al., 2006, 2016; Espley et al., 2004; Fowler et al., 2018; Lundin & Dubinin, 1992; Lundin et al., 2004; Pérez-de Tejada, 1987, 1998; Su et al., 2020; Wei et al., 2012; Xu et al., 2018).

Present-day Mars is a globally unmagnetized planet with multi-scale crustal magnetic anomalies predominantly in the southern hemisphere (Acuña et al., 1998; Connerney et al., 2005; Du et al., 2023). Due to the complex topology of these crustal fields and their interactions with the solar wind, their net effect on the escape of ionospheric heavy ions remains under debate. Observational analyses suggest that the southern hemisphere contributes approximately 46% ± 18% of the total global ion escape (Ramstad et al., 2016), with the influence of crustal magnetic fields ranging from a net decrease in ion escape of up to 40% to a net increase of about 20% (Weber et al., 2021). As supported by both observational studies (e.g., Dubinin et al., 2020; Lundin et al., 2011; Nilsson et al., 2011; Ramstad et al., 2016) and numerical simulations (e.g., Harnett & Winglee, 2005; Y.-J. Ma &

Nagy, 2007; Y. Ma et al., 2002, 2004; M. Wang et al., 2024), global ion escape rates show little correlation with the geometry of these crustal fields. These results indicate the presence of two competing effects. On one hand, crustal magnetic anomalies can form localized mini-magnetospheres that deflect solar wind flows (Fan et al., 2020; Harada et al., 2016; C. Zhang et al., 2024) and trap ionospheric heavy ions (Weber et al., 2021; C. Zhang et al., 2023). On the other hand, these same fields elevate plasma boundaries to regions of enhanced solar wind energy coupling (Cui et al., 2018; Dubinin et al., 2020), which may facilitate the escape of ionospheric plasma (Egan et al., 2019; Hanley et al., 2022). However, this conceptual framework leaves two critical questions unresolved: how solar wind energy penetrates the crustal magnetic barriers to reach the deep ionosphere, and through what topological pathways ion escape occurs within predominantly closed magnetic configurations.

In this study, based on observations by the Mars Atmosphere and Volatile EvolutioN mission (MAVEN) (Jakosky, Lin, et al., 2015), we propose a novel scenario for the escape of ionospheric heavy ions from the Martian crustal magnetic anomalies. The interaction between the crustal magnetic fields and the draped interplanetary magnetic fields leads to magnetic reconnection, which opens the crustal fields and creates magnetic cusp structures. The differential behavior of reconnection-accelerated ions and electrons within the magnetic anomaly creates a charge separation effect, establishing an ambipolar electrostatic potential. This potential structure preferentially accelerates ionospheric heavy ions along open magnetic field lines to escape altitudes, overcoming Martian gravity. This multi-stage escape scenario occurs within minutes and results in escape fluxes that are two orders of magnitude higher than the background levels.

2. Data and Instrumentation

The MAVEN spacecraft provided comprehensive data to understand the atmospheric loss on Mars (Jakosky, Lin, et al., 2015). The Magnetometer (MAG) (Connerney et al., 2015) measured the magnetic field vector with a sampling rate up to 32 Hz (Connerney, 2024). The Langmuir Probe and Waves (LPW) (Andersson et al., 2015) measured the electron density (Andersson, 2024), which was included in the MAVEN In Situ Instruments Key Parameters Data set (Dunn, 2024). The Solar Wind Electron Analyzer (SWEA) (Mitchell et al., 2016) measured the electron energy and pitch-angle distribution (Mitchell, 2023). The Supra-Thermal And Thermal Ion Composition (STATIC) instrument (McFadden et al., 2015) measured the velocity distribution and mass composition of ions (McFadden, 2024). The Solar Wind Ion Analyzer (SWIA) (J. S. Halekas et al., 2015) measured the ion velocity distribution (J. S. Halekas, 2024) under the assumption that only protons are present. Compared to STATIC, SWIA provided measurements extending to higher energies. Using the same algorithm as the Space Physics Environment Data Analysis System (SPEDAS) (Angelopoulos et al., 2019), we calculate the total densities and fluxes of O^+ and O_2^+ from STATIC measurements alone, while calculate the total densities and fluxes of H^+ from a combination of STATIC and SWIA measurements. The STATIC data were corrected for both spacecraft velocity (~4 km/s) and spacecraft potential (derived from STATIC measurements). MAVEN's orbital velocity during the event period enabled complete sampling of cold ions (<10 eV) along the ram direction, while STATIC's limited field-of-view (FOV) may introduce measurement biases for higher-energy ions (>30 eV). For SWIA data, only spacecraft velocity effects were corrected, as the analysis focused on high-energy ions (>494 eV) where spacecraft potential effects became negligible. However, SWIA's FOV constraints may similarly affect the measured high-energy ion distributions.

3. Event Overview

From 11:27 UT to 11:39 UT on 29 October 2015, MAVEN flew from its periapsis at ~160 km altitude toward higher altitudes up to ~560 km on dayside Mars (Figure 1a). Its trajectory, when mapped radially to Mars' surface, crossed the southern hemisphere with strong crustal magnetic fields (Figure 1b). The locally measured magnetic fields agreed well with the predictions of the crustal magnetic field model proposed by Gao et al. (2021) in both trends and magnitudes (Figure 1c). In the low-altitude region, the major ion species were O_2^+ and O^+ (Figure 1d). With increasing altitude, both ion densities decreased, and the relative proportion of O^+ increased (Figure 1d). The minor differences between LPW and STATIC measurements likely reflect instrumental effects: (a) LPW's Langmuir probe technique tends to yield slightly higher values than particle instruments in low-density plasma regimes (Andersson et al., 2015), while (b) STATIC experienced ion suppression during the event period (Figure 2b) (Fowler et al., 2022), reducing its sensitivity to low-energy ions. This combination of LPW's positive bias in low-density environments and STATIC's sensitivity limitations explains the observed measurement

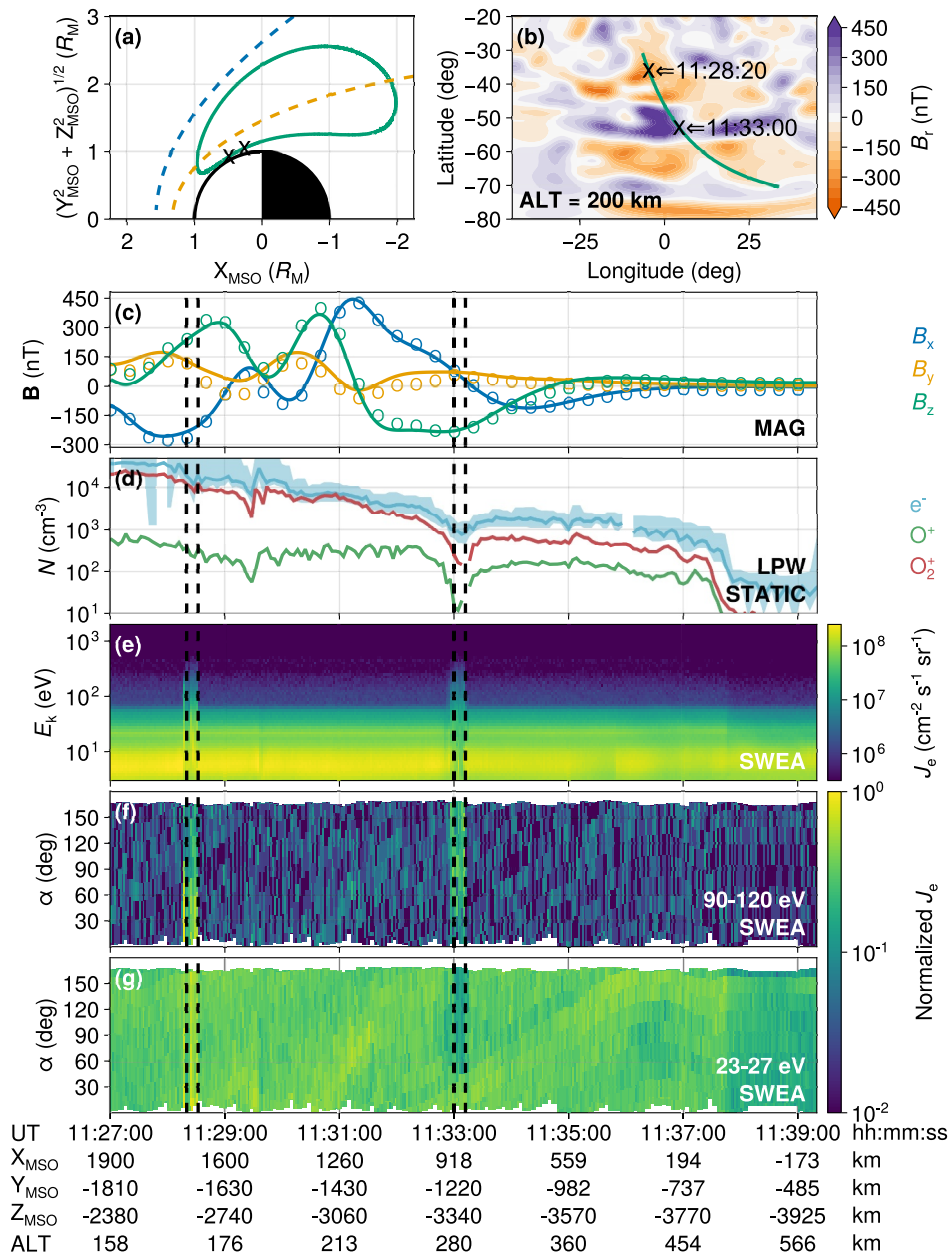

Figure 1. An overview of Martian mini-magnetospheric environment. (a) Trajectory (green solid line) of MAVEN in the Mars-centered Solar Orbital (MSO) cylindrical coordinate system. The blue and orange lines represent the bow shock and boundary of induced magnetosphere modeled empirically by Edberg et al. (2008). (b) Color-coded map of crustal radial fields modeled by Gao et al. (2021) at an altitude of 200 km, overlain by the trajectory of MAVEN (green solid line). In the panels (a) and (b), the two black cross symbols mark the crustal cusps around 11:28:20 and 11:33:00, respectively. (c) Observed (circles) and modeled (lines) magnetic fields in the MSO coordinate system. (d) Electron and ion densities. Colors help differentiate among particle species. The electron density profile includes a shaded region indicating its uncertainty range. (e) Electron differential energy flux (color-coded). (f) 23–27 eV and (g) 90–120 eV electron pitch angle distributions normalized to their respective maximum values (color-coded). In the panels (c)–(g), the vertical dashed lines mark the cusp regions with open magnetic field lines.

differences while preserving the physical interpretation of our results. Most of the time, MAVEN observed a clear photoelectron spectrum peak at 23–27 eV (Figure 1e), resulting from the ionization of CO_2 and O by the intense solar He-II emission (Frahm et al., 2006; Mantas & Hanson, 1979). These photoelectrons spread over the entire pitch angle range from 0° to 180° (Figure 1g), indicating closed magnetic field configurations (Brain et al., 2007;

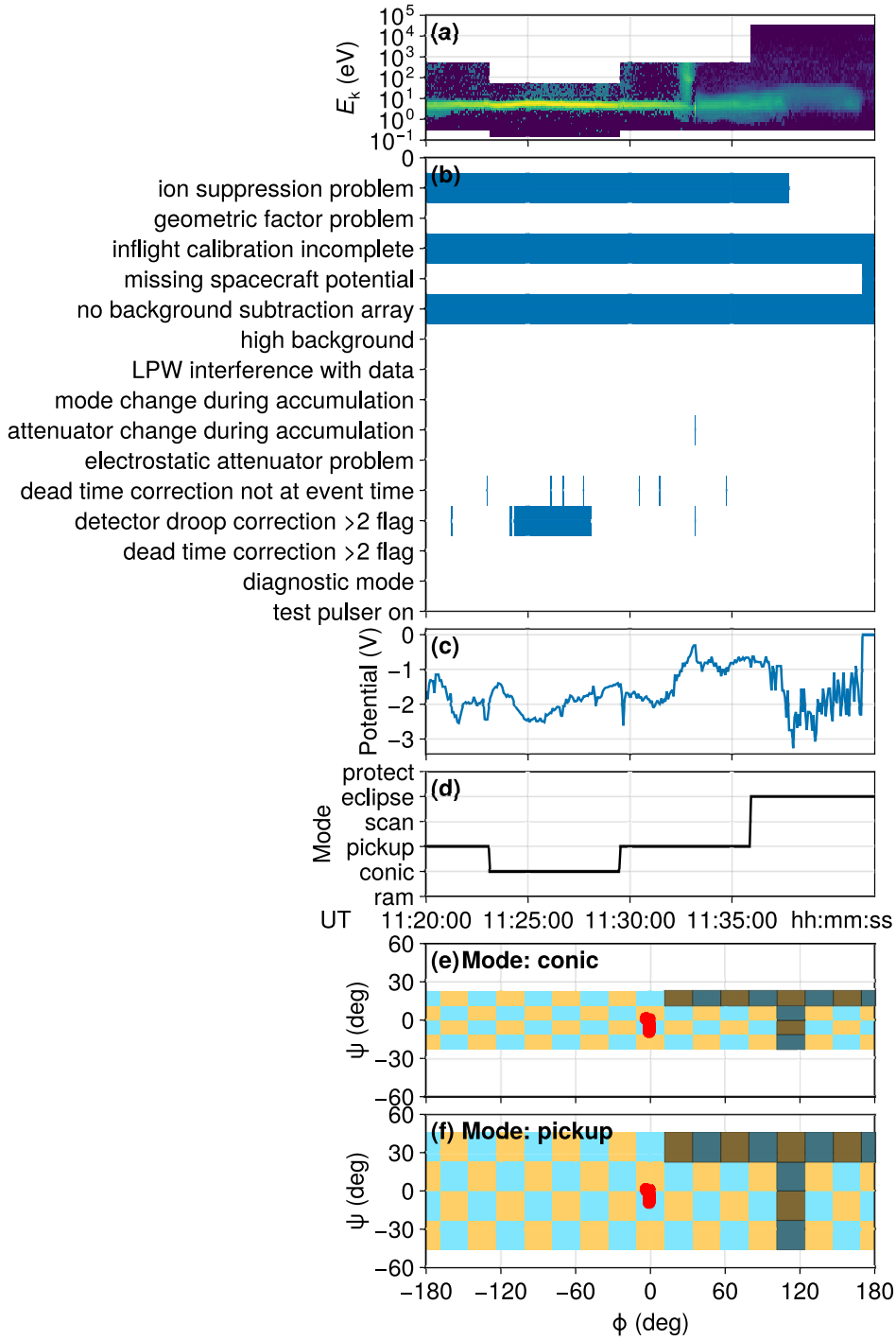

Figure 2. STATIC instrument status overview. (a) Ion energy spectra. (b) Data quality flag. (c) Spacecraft potential derived from STATIC C6 data product. (d) Instrument operational mode. (e), (f) Angular coverage and resolution of ion velocity distributions (Mercator Projection), with the instantaneous ram directions marked as red dots. Shadowed regions indicate angular sectors blocked by spacecraft components.

Xu et al., 2017). Around 11:28:20 UT and 11:33:00 UT, MAVEN detected injections of electrons of magnetosheath origin (with energies extending up to hundreds of eV) toward Mars (Figure 1e). Around 11:28:20 UT, the magnetic field lines were approximately pointed radially toward Mars ($B_r < 0$ in Figure 1b), and the injected electrons resided mainly in the pitch angle range of 0°–90° (Figure 1f). In contrast, around 11:33:00 UT, the

magnetic field direction reversed ($B_r > 0$ in Figure 1b), and the primary pitch angle range of injected electrons changed to 90°–180° (Figure 1f) and photoelectrons show a source cone distribution in the pitch angle range of 0°–30° (Figure 1g). These observations (marked by dashed lines in Figure 1) support an open magnetic field configuration, where one end is anchored in the ionosphere and the other end is connected to the interplanetary magnetic field (Brain et al., 2007; Xu et al., 2017). These approximately unipolar regions, characterized by strong (250–450 nT), vertical, and open magnetic fields (Figure 1b), can be considered crustal magnetic cusps (Krymskii et al., 2002; Lundin et al., 2006) by analogy to similar structures on the Earth.

Figure 3 displays the ion composition and energy spectra inside the two magnetic anomalies. Unlike the typical ionospheric populations below escape energies, there was an injection of suprathermal H^+, O^+, and O_2^+ approximately from 11:32:30 UT to 11:33:12 UT (Figures 3a–3j). The SWIA measurements (Figure 3g) revealed two distinct injection bands. The lower-energy band corresponded to the ion injection band detected by STATIC. As shown in Figures 3i and 3j, the injected O_2^+ and O^+ ions were predominantly below the upper energy limit of the STATIC instrument (494 eV). These injected O_2^+ ions exhibited a clear energy dispersive feature, whose central energy decreased from 200 to 70 eV within approximately 40 s. The O^+ injection had an energy band comparable to that of the O_2^+ injection. We therefore infer that, other than the H^+ injection within the energy range 30–494 eV measured by STATIC, the upper injection band (>494 eV), observed by SWIA, was primarily composed of H^+. The injected O_2^+ and O^+ ions of energies >30 eV measured by STATIC exhibited the peak fluxes close to the direction toward Mars (Figures 4a and 4b), similar to the ion measurements by SWIA at energies of 30–494 eV (Figure 4d). When the injected O_2^+ and O^+ ions were sufficiently dense (>1 cm^{-3}), their bulk velocities generally had angles with the Mars-ward direction in the range of 30° to 90° (Figures 4e, 4f and 5). In contrast, the injected H^+ ions showed a more diffuse velocity distribution (Figures 4c, 4d, and 6). When the injected H^+ ions were sufficiently dense (>1 cm^{-3}), their bulk velocities generally had angles with the Mars-ward direction in the range of 10° to 120° (Figures 4e and 4f). In fact, all the velocity distributions of these injected ions showed no significant clustering (Figures 5 and 6). The interpretation of reported bulk velocities requires careful consideration, as these values represent moment-based averages that may not fully capture the complex velocity-space structure of the injected plasma populations. The peak densities of injected O_2^+, O^+, and H^+ were roughly 35 cm^{-3}, 10 cm^{-3}, and 3 cm^{-3}, respectively (Figure 3l). These injected ions likely ionized neutral atoms through collisions, producing ions with energies of tens of eV (Gronoff et al., 2014). Along with the suprathermal ion injection (Figure 3l), there was a continuous decrease in the cold heavy ion densities (Figure 3k) on both closed and open field lines. The cusp ion densities around 11:33:00 UT were lower than those in the surrounding regions by approximately one order of magnitude. Crucially, STATIC maintained consistent operational modes and pointing directions throughout this period (Figures 2d–2f), effectively ruling out instrumental artifacts as the cause of this density drop. In contrast, for the magnetic cusp observed around 11:28:20 UT, with only a very weak injection of >1 keV ions likely of solar wind origin, the cold heavy ion densities showed little variation, nearly indistinguishable from the instrumental noise or natural fluctuations in density measurements (Figure 3e). These spatial and temporal correspondences imply that the cold heavy ion depletion was closely related to the suprathermal ion injection near the crustal cusp.

4. Discussion

4.1. Ionospheric Plasma Depletion Related to Magnetic Reconnection

C. Zhang et al. (2021) proposed that the precipitation of solar wind electrons might excite plasma waves which can subsequently heat the heavy ions and facilitate their escape. For the two magnetic cusps described here, with comparable intensity of solar wind electron precipitation, the cold heavy ions exhibited sharply different behavior. Therefore, the solar wind electron precipitation and subsequent wave-particle interaction was unlikely to be a major cause of the observed cold ion depletion here. Madanian et al. (2024) proposed that frictional heating can increase the ion temperature and enhance the charge exchange reaction rates, favoring recombination between ions and electrons, and ultimately leading to the formation of localized density depletion zones near crustal magnetic fields. However, this mechanism appears insufficient to explain why the depletion was predominantly confined to regions near the open field lines. Basuvaraj et al. (2022) demonstrated that Martian ionospheric plasma depletion events occur more frequently on the nightside compared to the dayside, with nightside depletions predominantly concentrated in the southern hemisphere. They proposed two plausible explanations: (a) plasma instabilities similar to those observed in Earth's ionosphere (e.g., Otsuka et al., 2002, 2021; Oya

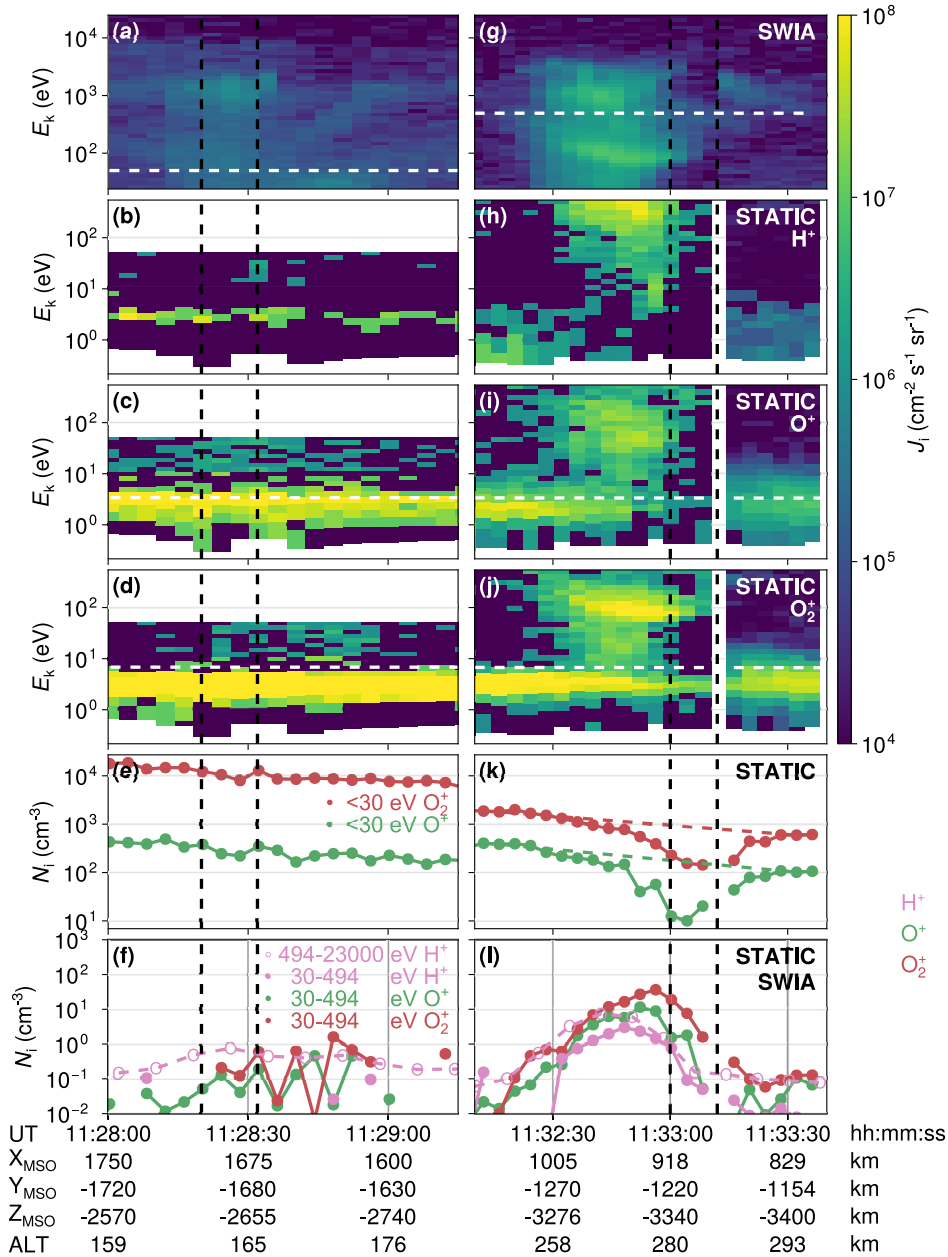

Figure 3. Comparison between two crustal magnetic anomalies without (left) and with (right) substantial suprathermal ion injections. (a), (g) Ion differential energy flux measured by SWIA. The horizontal dashed lines indicate the upper energy boundary of STATIC measurements. (b–d, h–j) H^+, O^+ and O_2^+ differential energy fluxes measured by STATIC. A data gap related to the engaging mechanical attenuator changing the instrument sensitivity during a measurement was observed around 11:33:12. In the panels (c, d, i, j), the white dashed lines mark the corresponding ion escape energies. (e), (k) Cold (<30 eV) ion densities measured by STATIC. In the panel (k), the colored dashed lines represent the undisturbed altitude-dependent trends of ion densities. (f, l) Suprathermal (>30 eV) ion densities measured by STATIC (solid lines with dots) and SWIA (dashed lines with circles). In the panels (e, f, k, l), colors help differentiate among ion species. In all those panels, the vertical dashed lines mark the cusp regions with open magnetic field lines.

et al., 1986), and (b) localized plasma heating by energetic protons and electrons. In contrast, the ionospheric plasma depletion described here was closely related to an injection of a mixture of predominantly heavy ions and fewer protons. The injected heavy ions were likely of ionospheric origin, whereas the injected protons were predominantly from the solar wind. Given that the background ionospheric heavy ions had thermal energies below 10 eV, an acceleration mechanism was required to account for the observed suprathermal heavy ion

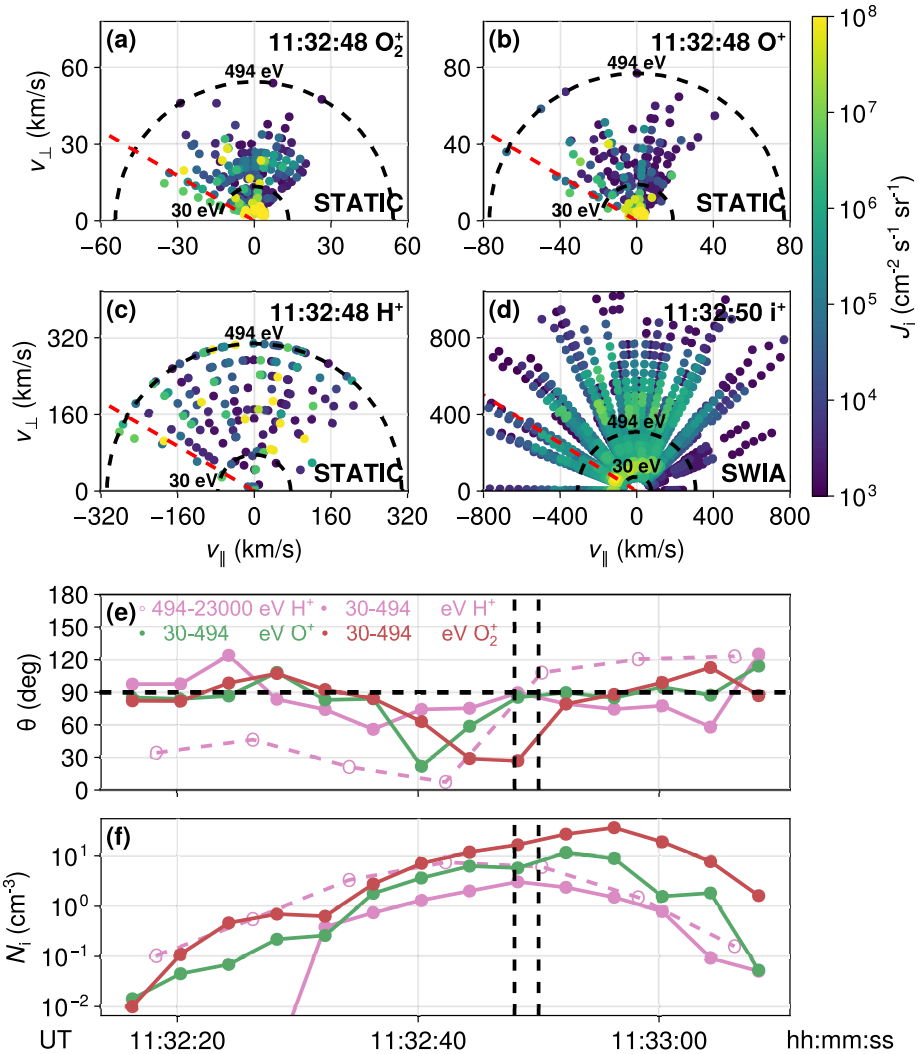

Figure 4. Ion velocity distributions. (a–c) STATIC measurements of O_2^+, O^+, and H^+ in the cylindrical field-aligned coordinate system. (d) SWIA undifferentiated ion measurements in the same coordinate system. Red dashed lines indicate the direction toward Mars, and black dashed circles mark energy levels at 30 and 494 eV. (e) Angle between Marsward direction and instantaneous bulk velocity of injected ions. (f) Injected ion densities. In panels (e and f), colors help differentiate among ion species, and dashed vertical lines mark the time moments corresponding to panels (a–d).

injection. In light of the magnetic field reconfiguration and the mixing of ions from both sources, this suprathermal ion injection can be interpreted as a jet resulting from magnetic reconnection (e.g., Chen et al., 2023; Harada et al., 2018; J. Wang et al., 2021; Ye et al., 2024). Ye et al. (2024) reported Martian ionospheric plasma depletions caused by reconnections involving open, oppositely directed, strong crustal magnetic field lines. Their analysis indicates that the outer ionospheric plasma was expelled outward due to the tension force exerted by the reconnected magnetic field lines. Unlike the event reported by Ye et al. (2024), the ionospheric plasma depletion observed in this study was accompanied by an ion jet directed toward Mars (Figures 4a and 4b) and occurred in the low-altitude region (280 km). Given the approximately unipolar nature of the crustal magnetic field, we speculate that the reconnection involved interactions between the crustal magnetic fields and the draped interplanetary magnetic fields. Such reconnection events can produce open magnetic field lines, with one end anchored in the ionosphere and the other connected to the interplanetary magnetic field.

During the time period of interest, MAVEN's orbital trajectory was downstream of the bow shock (Figure 1a). Measurements from a single spacecraft cannot effectively distinguish spatial variations from temporal changes in the magnetic field. It is challenging to accurately determine the orientation of the draped interplanetary magnetic

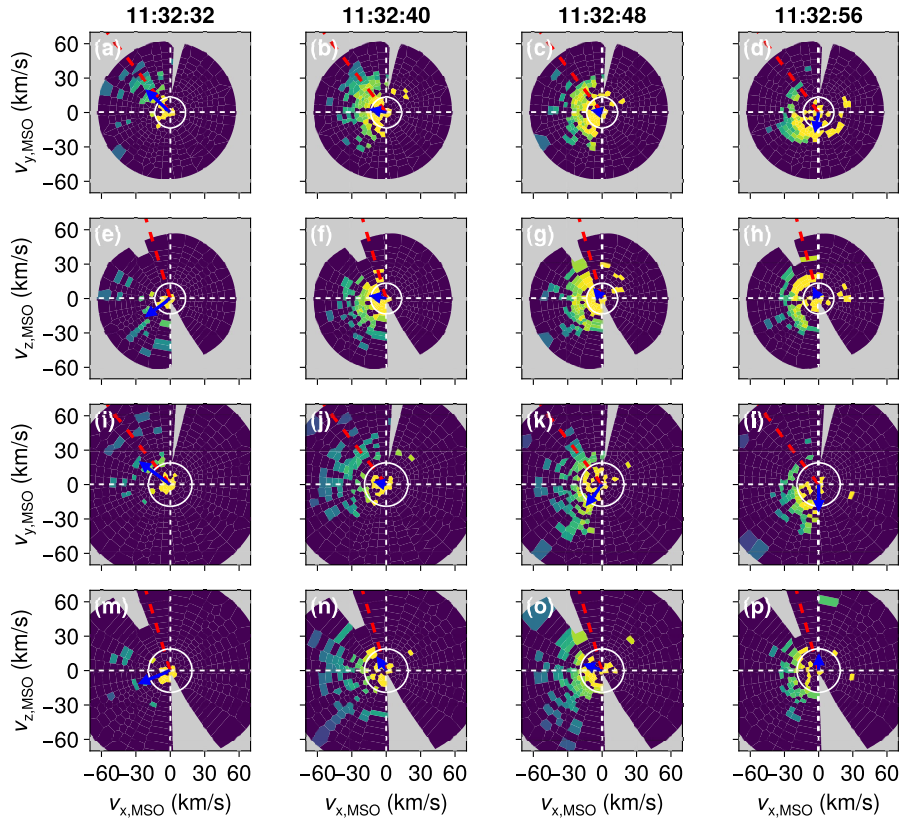

Figure 5. Ion velocity distributions measured by STATIC in MSO coordinates. (a–h) Two-dimensional slices of O_2^+, distributions in the $V_{x,MSO}$–$V_{y,MSO}$ and $V_{x,MSO}$–$V_{z,MSO}$ planes at selected times. (i–p) Corresponding O^+ distributions in the same coordinate planes. Gray-shaded regions indicate coverage gaps caused by both instrument blind spots and spacecraft structural blockage. Red dashed lines indicate the direction toward Mars, blue arrows mark the projected bulk velocities of injected ions (>30 eV), and white circles represent the energy level at 30 eV.

field. Following our previous study (Cheng et al., 2024), we reluctantly infer that the draped interplanetary magnetic field may be approximately aligned with the discrepancy between the modeled (Gao et al., 2021) and observed magnetic fields. Throughout the strong cusp region sampled by MAVEN from 11:28:20 UT to 11:33:00 UT, this discrepancy was spatially stable (Figures 7b and 7e), with an average value of $\Delta\mathbf{B} = (-15, -50, 25)$ nT in the Mars-centered Solar Orbital (MSO) coordinate system (Figure 7b).

Considering that the ion acceleration primarily occurs near the reconnection site, we believe that the ion density at the reconnection site was at least as high as the density of the injected suprathermal ions (35 cm^{-3} for O_2^+). As illustrated in Figure 7a, the ionopause was located at approximately 490 km altitude (black dashed line in Figure 7a), above which the ion density decreased rapidly from ~100 to 10 cm^{-3} over a 30 km altitude range. Based on these observations, we speculate that the reconnection site was situated near the ionopause (at 490 km altitude).

4.2. Differential Penetration of Ions and Electrons From Magnetic Reconnection

As modeled by Gao et al. (2021), the magnetic cusp exhibits a magnetic field structure diverging from the center outward (Figure 8a). Near the ionopause, the shear angles between the crustal magnetic fields and the draped interplanetary magnetic fields range approximately from 0° to 180°. Analogous to Earth's magnetosphere, this Martian mini-magnetosphere may have one or more reconnection lines (Cowley, 1976; Fuselier et al., 2018; Moore et al., 2002; Trattner et al., 2021), along which the shear angles are not always close to 180° but extend down to 90°. Using the crustal field model proposed by Gao et al. (2021), we have identified two representative magnetic field lines that may have participated in the reconnection process. Both field lines originate near the observed cusp and extend to a peak altitude of approximately 490 km. The corresponding shear angles are 102° (Figure 8b) and 137°

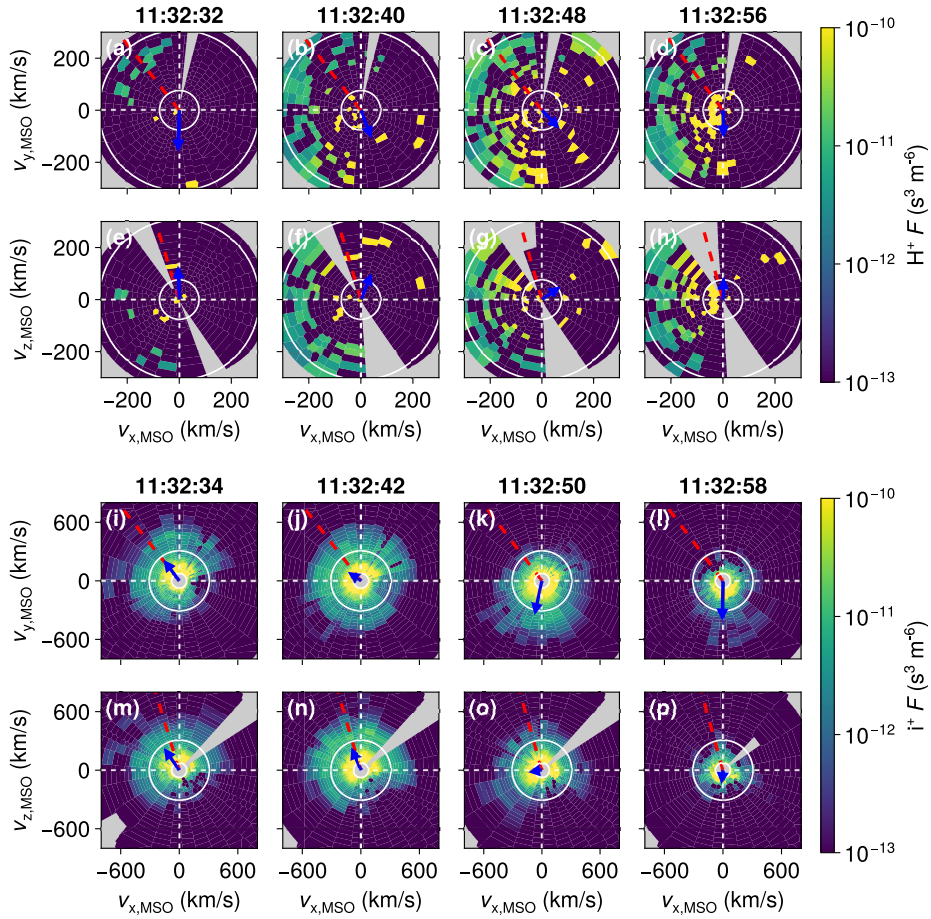

Figure 6. Same format as Figure 5, showing (a–h) STATIC H^+ and (i–p) SWIA undifferentiated ion measurements. Bulk velocities (blue arrows) were calculated for $E > 30$ eV H^+ (panels a–h) and $E > 494$ eV ions (panels i–p). White circles mark the reference energy levels at 30 and 494 eV, respectively.

(Figure 8c). According to the component reconnection theory (Cowley, 1976; Moore et al., 2002), under the assumption of equivalent magnitudes of the crustal and draped interplanetary magnetic fields near the reconnection site, the two reconnection jets flow along the midline of the two reconnecting magnetic field lines. In other words, the reconnection jet velocity $\mathbf{V}_{jet}$ aligns with $\pm(\mathbf{e}_{IMF} + \mathbf{e}_{Crustal})$, where $\mathbf{e}_{IMF}$ and $\mathbf{e}_{Crustal}$ are unit vectors along the interplanetary and crustal magnetic fields, respectively. Specifically, for the first reconnection configuration, the directions of the two reconnection jets are $(\mp 0.77, \mp 0.64, \pm 0.07)$ in the MSO coordinate system; for the second reconnection configuration, these jet directions become $(\mp 0.84, \mp 0.46, \mp 0.31)$.

To investigate the migration of the reconnection jet, we perform test-particle simulations. For simplicity, these simulations do not account for the reconnection-related electric field or any potential reconfiguration of the magnetic field structure resulting from the reconnection process. Test particles are initialized with velocities parallel to the Mars-ward reconnection jet at the presumed reconnection site. Their motions are determined by the following equations:

$$\frac{d\mathbf{r}}{dt} = \mathbf{v}, \tag{1}$$

$$\frac{d\mathbf{v}}{dt} = \frac{q}{m}\mathbf{v} \times \mathbf{B}, \tag{2}$$

where $\mathbf{r}$, $\mathbf{v}$, q, and m are the position vector, velocity, charge, and mass of the test particles, respectively, and $\mathbf{B}$ is the static crustal magnetic field modeled by Gao et al. (2021).

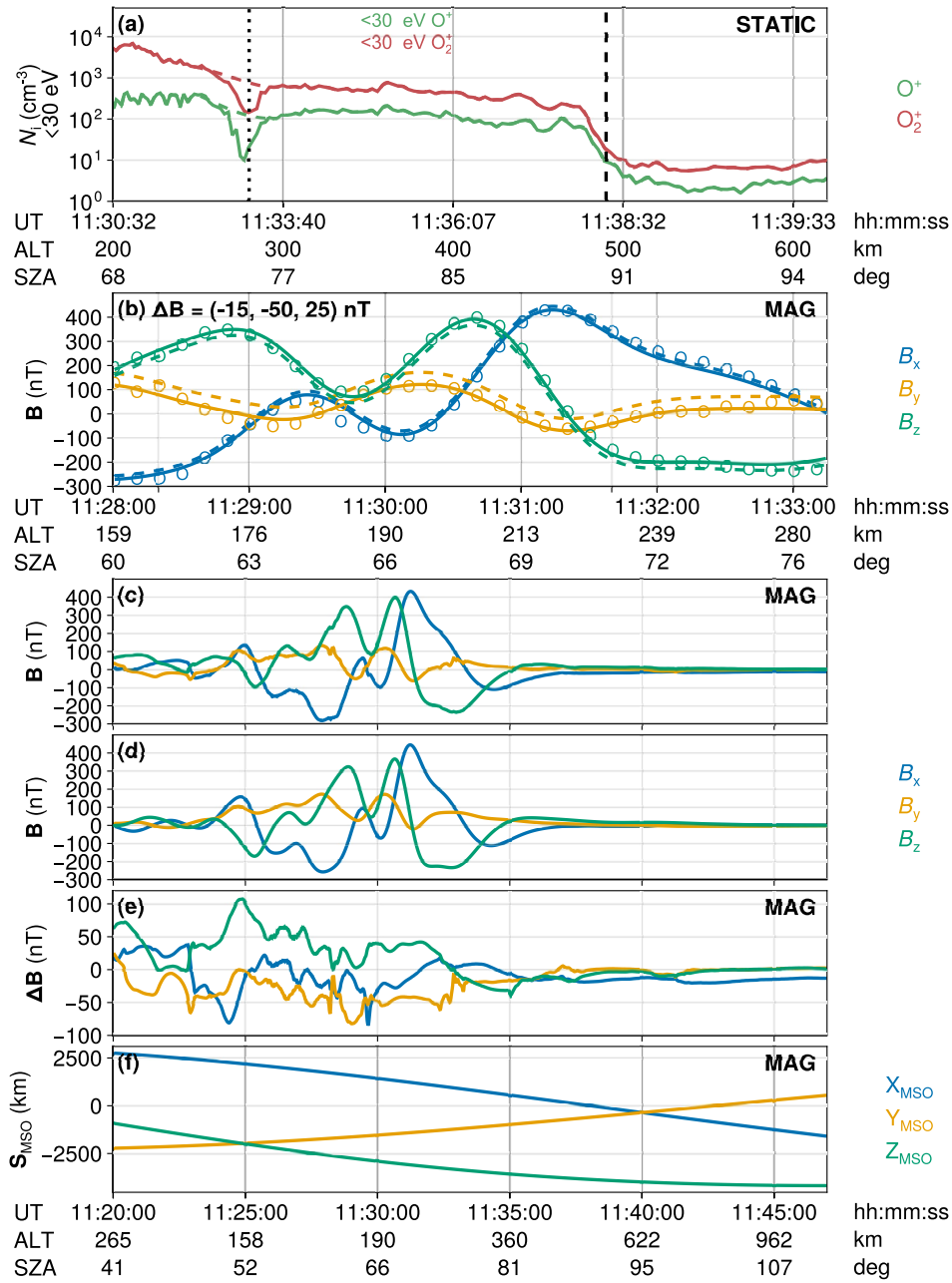

Figure 7. Background conditions for magnetic reconnection. (a) Altitude-dependent cold (<30 eV) ion densities. The colored dashed lines represents the undisturbed trends. The black dotted and dashed lines mark the cusp and the ionopause, respectively. (b) Difference between observed and modeled magnetic fields near the magnetic cusp in the MSO coordinate system, with circles for the actual measurements, dashed lines for the values from the model (Gao et al., 2021), and solid lines for the updated modeled values with an added perturbation of $\mathbf{\Delta B} = (-15, -50, 25)$ nT. (c)–(f) Comparison between observed and modeled magnetic fields in MSO coordinates over an extended time period. (c) Magnetic field measurements. (d) Crustal magnetic field modeling results (Gao et al., 2021). (e) Difference between observations and model. (f) MAVEN trajectory in the MSO coordinate system.

For the first reconnection configuration shown in Figures 8b, 8d, 8f and 8h, test electrons with energies ranging from 10 eV to several keV are always trapped within the high-altitude (~400 km) regions of the magnetic field lines. In real situations with open field lines, the electrons would be reflected away from the magnetic anomaly. In contrast, the higher the ion energy, the lower the altitude they can reach. This is because the magnetic field strength generally increases as altitude decreases. Ions require sufficiently large energies to enlarge their

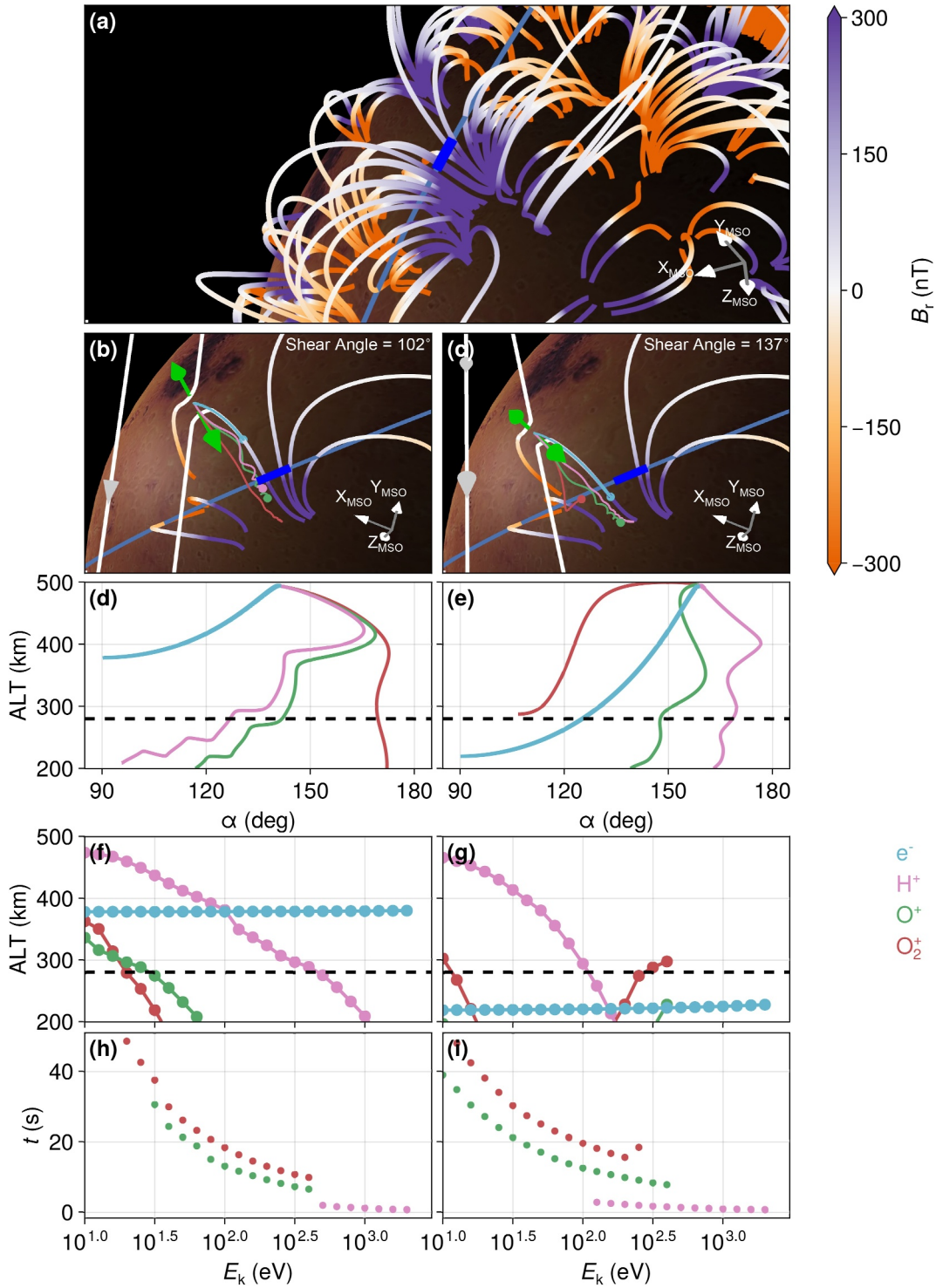

Figure 8. Inferred magnetic reconnection process. (a) Three-dimensional crustal magnetic field lines modeled by Gao et al. (2021), with field line colors indicating the strength of the radial magnetic component. The blue line shows MAVEN's trajectory, with the bold segment marking the suprathermal ion injection region. (b), (c) Schematic diagrams of the three-dimensional reconnection configuration: white lines represent interplanetary magnetic fields; green arrows indicate reconnection jets; colored trajectories represent test particles (pink: 1,000 eV H^+; green: 85 eV (b) and 155 eV (c) O^+; red: 171 eV (b) and 311 eV (c) O_2^+; light blue: 50 eV e^-). (d), (e) Pitch angles of test particles. (f), (g) Energy-dependent injection depths of test particles. (h), (i) Energy-dependent injection times of test particles. In the panels (d)–(g), the black dashed line indicates MAVEN's altitude. In the panels (d)–(i), colors help differentiate among particle species.

gyroradii, allowing them to penetrate deeper into regions of stronger magnetic fields. To reach the altitude where MAVEN was located (approximately 280 km), the threshold energies are estimated to be approximately 500 eV for H^+, 30 eV for O^+, and 20 eV for O_2^+. Using plausible but unverified parameters near the reconnection site (ion compositions of 7.9 cm^{-3} O^+ and 19.9 cm^{-3} O_2^+ from Figure 7; background magnetic field of 40.5 nT from the model (Gao et al., 2021)), we derive an indicative Alfvén velocity of 32 km/s. These values should be considered illustrative rather than definitive. O_2^+ and O^+ of ionospheric origin have relatively low velocities before reconnection and approximately acquire the Alfvén velocity in the reconnection jet. Their corresponding energies are estimated to be around 171 eV for O_2^+ and 85 eV for O^+. As for H^+ of solar wind origin, which typically has an initial energy in the keV range, the additional energy imparted by reconnection is negligible. These calculations support that the reconnection jet has sufficient energy to reach MAVEN, and the observations also confirmed the existence of such ion injection (Figures 3h–3j). In the second reconnection configuration shown in Figure 8c, the velocity magnitude of the reconnection jet, 43 km/s, is comparable to that in the first configuration. However, due to the increased shear angle, the test electrons have an initial pitch angle close to ∼160°, allowing them to penetrate down to altitudes below 280 km. In real situations, these electrons would be reflected at low altitudes and eventually escape along the open magnetic field lines on a timescale of tens of milliseconds. The subsequent ion injection, which occurs over a much longer timescale, resembles that described for the first configuration. Note that the penetration altitude does not exhibit a simple anti-correlation with O_2^+ energy due to the complex magnetic field configuration and non-adiabatic cross-field ion transport (Figure 8g).

We emphasize that our magnetic reconnection model is intentionally simplified and not intended to quantitatively reproduce all observational details. Rather, its purpose is to demonstrate the fundamental viability of the proposed mechanism. At the altitude of MAVEN, pitch angles of test O_2^+ and O^+ ions under both reconnection configurations range from 100° to 160° (Figures 8d and 8e), which is qualitatively consistent with observations (Figure 4). Because of the deflection by the crustal magnetic field, the velocity vectors of the test O_2^+ and O^+ ions vary with altitude (Figure 9). In other words, far away from the reconnection site, the injected ion velocity vectors can differ substantially from the initial reconnection jet directions. Particularly at the MAVEN altitude, these ions have gyro-radii of 5–10 km and gyro-periods of 5–10 s. Within a single gyro-period, they can travel approximately 100 km in altitude, while the spacecraft moves 20–40 km horizontally. Meanwhile, O_2^+ and O^+ ions accelerated from magnetic reconnection at different spatial and temporal locations may be sampled by the spacecraft simultaneously. The finite gyroradius effect and the potential mixing of multiple ion jets could explain the observed lack of significant clustering in the phase space density of injected O_2^+ and O^+ ions (Figure 5), as well as the broad distribution of instantaneous velocity vectors (Figure 9). The velocity of H^+ is primarily derived from the solar wind itself rather than from the magnetic reconnection. As a result, the observed suprathermal H^+ exhibited a more diffuse velocity distribution (Figures 4c and 4d). The transit times of test ions from the reconnection site to the altitude of 280 km depends on their energies. Specifically, ∼200 eV O_2^+ arrives ∼13 seconds earlier than ∼50 eV O_2^+, qualitatively explaining the observed energy-dispersive structure of injected ions (Figure 3j). MAVEN observed higher densities of injected ions in the closed field region compared to the open field region (Figure 3l), which may not reflect a spatial distribution feature but rather a coincidence in timing. The reconnection event may have lasted for about 1 minute in a non-steady manner, with the ion injection rate peaking when MAVEN was within the closed field region. In the low-altitude region with strong crustal magnetic fields, the closed field topology is more prevalent than the open field topology. Therefore, MAVEN had more opportunities to make measurements in the closed field configuration. As revealed by the simulations (Figures 8b and 8c), the test ions, depending on the shear angle of magnetic reconnection, do not always follow the open field lines but can extend into the closed field region, and they are not always confined at the MAVEN altitude but can propagate to lower altitudes. During their atmospheric propagation, these particles can be expected to gradually lose energy through multiple physical processes including collisional interactions and wave-particle interactions. Eventually, some of these ions may become trapped in strong crustal magnetic fields at low latitudes, while others may be reflected back to higher altitudes. This bifurcation depends sensitively on both the particles' initial velocities and the local magnetic field geometry they encounter during propagation. The injected H^+ ions with keV-level energies reach the MAVEN altitude much earlier than the injected O_2^+ and O^+ ions (Figures 8h and 8i), qualitatively explaining the observed difference in arrival times of the peak densities of H^+, O^+, and O_2^+ (Figure 4f). At the late stage, the bulk velocities of those H^+ ions with energies >494 eV exhibited angles up to 120° relative to the Mars-ward direction (Figure 4e), which may be interpreted as a signature of reflected H^+ detection. As for the suprathermal electrons observed concurrently (Figure 1f), they may not have

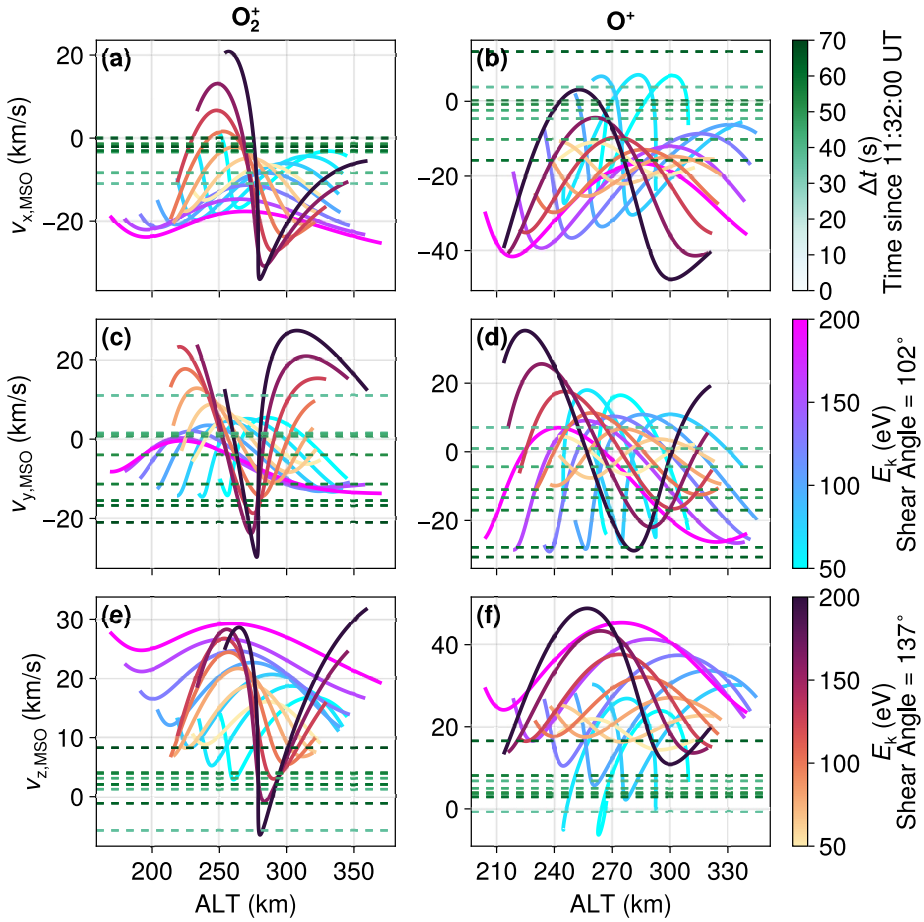

Figure 9. Comparison of observed and modeled injected ion velocities. Rows 1–3 show velocity components along the MSO x, y, and z axes, respectively. Left and right columns display O_2^+ and O^+ results. Horizontal dashed lines indicate the calculated bulk velocities of injected ions (>30 eV and >1 cm^{-3}), with color saturation encoding time elapsed since 11:32:00 UT. Solid curves show modeled velocities for ions with different initial energies (color-coded) from various reconnection configurations (labeled), tracked for approximately one gyroperiod near MAVEN's altitude.

originated from the impulsive reconnection jet, but could instead be persistent solar wind electrons moving antiparallel to the open magnetic field lines. For both reconnection configurations, the charge separation can be expected to generate a complex electric field system throughout the entire magnetic anomaly (e.g., Y. Dong et al., 2024; Poppe et al., 2021; Xu et al., 2018). This newly generated electric field could induce spatial transport of cold heavy ions in regions with closed field lines, while facilitating their loss in regions with open field lines. Although without available observations, previous simulations did support the generation of a potential drop of several to hundreds of Volts over a 200 km height along the open field lines (e.g., Y. Dong et al., 2024; Poppe et al., 2021). Such a potential drop could effectively drive the escape of cold heavy ions through the cusp.

At lunar magnetic anomalies, the finite gyroradius effect of solar wind ions has been proposed as a mechanism for building up an electrostatic potential (Deca et al., 2016; Futaana et al., 2013; J. Halekas et al., 2011; Lue et al., 2011; Poppe et al., 2012; Saito et al., 2012). There are two major differences between the Martian and lunar scenarios. The first is the species of ions injected into the magnetic anomalies. The second is whether magnetic reconnection is involved in the process. At the Moon, solar wind protons have sufficient energy to penetrate the magnetic anomaly; in contrast, at Mars, background heavy ions must be accelerated by magnetic reconnection before they can penetrate the magnetic anomaly.

4.3. Charge Equality of Injected and Outflowing Ions

Under the hypothesis of this electrostatic extraction mechanism, as ionospheric ions are progressively extracted, the electrostatic field gradually weakens. Ideally, charge equality between injected and outflowing ions serves as a criterion for evaluating the efficiency of electrostatic extraction mechanisms. Since the ions involved typically carry only a single positive charge, charge equality corresponds to the equality of the total number of ions. To test this hypothesis, we estimate both the number of outflowing ions and the number of injected ions.

The total number of outflowing ions may be estimated as:

$$Q_{\text{out}} = \int_{h_1}^{h_2} \Delta N_{\text{i}}(h) A_{\text{out}}(h) \mathrm{d}h, \tag{3}$$

$$A_{\text{out}}(h) = A_{\text{out}}(h_1) \frac{B_{\text{r}}(h_1)}{B_{\text{r}}(h)}, \tag{4}$$

where h_1 is the altitude MAVEN was located at (280 km), h_2 is the inferred reconnection altitude (490 km), $\Delta N_{\text{i}}(h)$ is the net decrease in ion density, $A_{\text{out}}(h)$ is the altitude-dependent cross-sectional area of the tube with open magnetic fields, and $B_{\text{r}}(h)$ is the altitude-dependent radial magnetic field modeled by Gao et al. (2021). Given the inherent limitations of single-spacecraft observations, we conservatively estimate the ion depletion region to span altitudes from $h_1 = 280$ km to $h_2 = 490$ km. The lower limit h_1 corresponds to the minimum altitude where clear depletion signatures were observed, while the upper limit h_2 approximates the ionopause location at Mars. Although the actual depletion layer may extend beyond these boundaries, this constrained altitude range serves as a robust baseline for quantifying the total population of outflowing ions. We approximate $A_{\text{out}}(h_1) = 2,281$ km^2 as the square of the spacecraft's horizontal displacement from 11:33:00 UT to 11:33:12 UT. Within this time period, the averaged net decrease in ion density is $\Delta N_{\text{i}}/N_{\text{i}} = 0.82$, where N_{i} (colored dashed lines in Figure 7a) is the inferred ion density before reconnection. The obtained total number of outflowing ions is $Q_{\text{out}} \approx 3.14 \times 10^{23}$. In addition to the ion depletion observed on the open magnetic field lines, part of the ions on neighboring closed field lines could also transport toward the cusp due to the thermal pressure gradient and the newly generated electric field system (Figure 3k). Our calculation likely underestimates the number of outflowing ions to some extent.

The total number of injected ions may be estimated as:

$$Q_{\text{in}} = A_{\text{in}}(h_1) \int_{t_1}^{t_2} F_{\text{in}}(t, h_1) \cos(\pi - \theta_{\text{in}}(t)) \, \mathrm{d}t, \tag{5}$$

where t_1 and t_2 are the start and end times of injection, $F_{\text{in}}(t, h_1)$ is the injected ion flux at $h = h_1$, $\theta_{\text{in}}(t)$ is the angle between the injected ion flux and the background magnetic field, and $A_{\text{in}}(h_1)$ is the cross section perpendicular to the background magnetic field at $h = h_1$. In this specific region, the magnetic field lines were approximately directed radially outward from Mars. According to observations, we specify the injection time from $t_1 =$ 11:32:16 UT to $t_2 =$ 11:33:12 UT. We approximate $A_{\text{in}}(h_1) = 50,691$ km^2 as the square of the spacecraft's horizontal displacement during this injection time period. With the injection flux and angle shown in Figures 10b and 10c, we obtain the total number of injected ions $Q_{\text{in}} \approx 4.99 \times 10^{23}$. The actual distribution of injected ions may vary spatially, which cannot be determined with observations from a single spacecraft. The limited FOVs of both STATIC and SWIA may lead to an underestimation of the injected ion number. Based on the assumption of homogeneous ion injection over the entire region $A_{\text{in}}(h_1)$, our estimate may not fully capture the true complexity of the ion injection process.

Estimations based on available observations suggest that the number of ions injected into the system was comparable to the number of outflowing ions observed. However, the injected ions were scattered over a volume tens of times larger than the volume of outflowing ions where the magnetic field lines were open. Therefore, the localized ionospheric plasma depletion became observable.

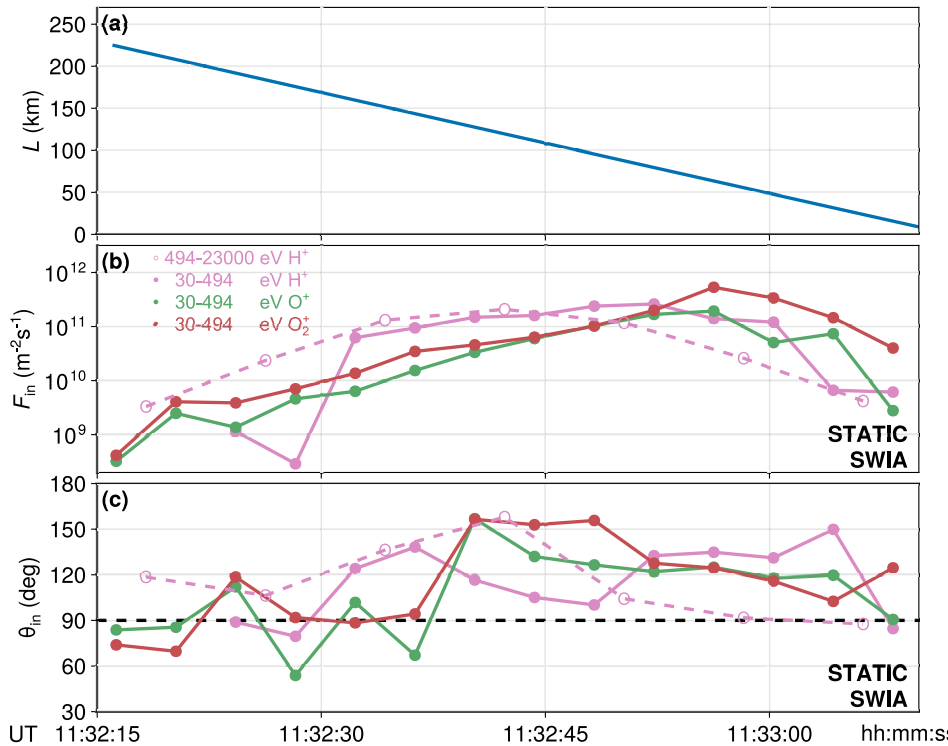

Figure 10. Spatiotemporal characteristics of suprathermal ion injection. (a) Horizontal displacement of MAVEN relative to its position at 11:33:12 UT. (b) Injected ion fluxes. (c) Corresponding angles between the injected ion fluxes and the background magnetic field. Colors help differentiate among ion species. Note that H^+ measurements were provided by STATIC (solid lines with dots) and SWIA (dashed lines with circles) in different energy ranges, whereas O^+ and O_2^+ measurements were provided exclusively by STATIC.

5. Summary

In this study, we present a new mechanism for the escape of ionospheric heavy ions from the crustal magnetic anomalies on Mars. The interplanetary magnetic fields drape around Mars and undergo reconnection with the crustal magnetic fields, leading to the formation of magnetic cusps with open field lines and generating jets that impact these magnetic anomalies. Due to the significant difference in gyroradius and velocities between ions and electrons, the injected ions and electrons exhibit distinct spatial and temporal behaviors. This charge separation results in the buildup of electrostatic potential within the cusps, which subsequently extracts cold heavy ions from the ionosphere to higher altitudes. MAVEN observations have demonstrated the close relationship between transient suprathermal ion injection and localized ionospheric depletion, and calculations confirm the charge equality of injected and extracted ion populations. For the specific event reported here, the entire physical process chain completed in approximately 1 minute, with about 3.1×10^{23} heavy ions escaping through a cross-sectional area of roughly $2,281$ km^2. The corresponding escape flux reached 3.0×10^{18} km^{-2}s^{-1}, which is approximately two orders of magnitude higher than the globally averaged escape flux during quiet times (Jakosky, Grebowsky, et al., 2015).

While this study establishes a causal chain from magnetic reconnection to ionospheric heavy ion escape, it also highlights several significant limitations. First, the entire physical process spans an altitude range of more than 200 km within a single minute, making it impossible for a single spacecraft to simultaneously observe all involved phenomena. For the specific event reported here, MAVEN was at a relatively low altitude, enabling the detection of ion injection but not magnetic reconnection itself. Second, there is currently no comprehensive, self-consistent physical model that fully captures all aspects of this process. Previous modeling studies (e.g., Poppe et al., 2021; Y. Dong et al., 2024) have characterized electrostatic potential buildup in idealized magnetic cusp configurations under steady ion injection conditions. However, significant challenges remain in modeling the complete electric field system associated with transient ion injection events within realistic, complex magnetic topologies. At least

two key difficulties arise: (a) the dynamic coupling between time-varying plasma populations and evolving field structures; (b) the computational limitations in simulating three-dimensional, non-equilibrium configurations with sufficient resolution. Third, given the explosive nature of the phenomenon, conducting a statistical analysis to evaluate its universality and overall importance remains challenging. Despite these limitations, the proposed mechanism may serve as a candidate explanation for how ionospheric heavy ions can escape from regions with strong crustal magnetic anomalies. This explosive leakage pattern could be generalized to other planets where magnetospheric and ionospheric boundaries converge. On Earth, by contrast, with the vast separation between the ionosphere and the magnetopause (~60,000 km), the solar wind drives the escape of ionospheric heavy ions through a more complex interplay involving magnetopause reconnection and wave-particle interactions (H. Zhang et al., 2022, 2023).

Data Availability Statement

Data used in study is available on the NASA Planetary Data System (https://pds-ppi.igpp.ucla.edu/search/default.jsp). In this work, we have analyzed the following data: (a) L2 MAG data (Connerney, 2024); (b) MAVEN In Situ Key Parameters (Dunn, 2024); (c) L2 SWEA data (Mitchell, 2023); (d) L2 STATIC data (McFadden, 2024). (e) L2 SWIA data (J. S. Halekas, 2024).

Acknowledgments
We acknowledge the entire MAVEN team for providing data. This work was supported by the National Natural Science Foundation of China Grants 42130204, 42441808, 42188101, 42274198 and 42441829, the Postdoctoral Fellowship Program of China Postdoctoral Science Foundation GZB20240701 and the open project fund of State Key Laboratory of Lunar and Planetary Sciences 002/2024/SKL.

References

Acuña, M. H., Connerney, J. E. P., Wasilewski, P., Lin, R. P., Anderson, K. A., Carlson, C. W., et al. (1998). Magnetic field and plasma observations at Mars: Initial results of the Mars Global Surveyor mission. *Science*, *279*(5357), 1676–1680. https://doi.org/10.1126/science.279.5357.1676

Andersson, L. (2024). *MAVEN LPW calibrated data bundle*. NASA Planetary Data System. https://doi.org/10.17189/1414175

Andersson, L., Ergun, R. E., Delory, G. T., Eriksson, A., Westfall, J., Reed, H., et al. (2015). The Langmuir Probe and Waves (LPW) instrument for MAVEN. *Space Science Reviews*, *195*(1–4), 173–198. https://doi.org/10.1007/s11214-015-0194-3

Angelopoulos, V., Cruce, P., Drozdov, A., Grimes, E. W., Hatzigeorgiu, N., King, D. A., et al. (2019). The space physics environment data analysis system (SPEDAS). *Space Science Reviews*, *215*(1), 9. https://doi.org/10.1007/s11214-018-0576-4

Basuvaraj, P., Němec, F., Němeček, Z., & Šafránková, J. (2022). Ionospheric plasma depletions at Mars observed by the MAVEN spacecraft. *Journal of Geophysical Research: Planets*, *127*(11), e2022JE007302. https://doi.org/10.1029/2022JE007302

Brain, D. A., Lillis, R. J., Mitchell, D. L., Halekas, J. S., & Lin, R. P. (2007). Electron pitch angle distributions as indicators of magnetic field topology near Mars. *Journal of Geophysical Research*, *112*(A9), 2007JA012435. https://doi.org/10.1029/2007JA012435

Brain, D. A., McFadden, J. P., Halekas, J. S., Connerney, J. E. P., Bougher, S. W., Curry, S., et al. (2015). The spatial distribution of planetary ion fluxes near Mars observed by MAVEN. *Geophysical Research Letters*, *42*(21), 9142–9148. https://doi.org/10.1002/2015GL065293

Chen, G., Huang, C., Zhang, Y., Ge, Y., Du, A., Wang, R., et al. (2023). MAVEN observations of the interloop magnetic reconnections at Mars. *Astrophysical Journal*, *952*(1), 37. https://doi.org/10.3847/1538-4357/acda90

Cheng, S., Su, Z., Wu, Z., & Wang, Y. (2024). Inferring whistler-mode chorus wave source regions in the Martian mini-magnetospheres. *Geophysical Research Letters*, *51*(2), e2023GL106695. https://doi.org/10.1029/2023GL106695

Collinson, G., Glocer, A., Xu, S., Mitchell, D., Frahm, R. A., Grebowsky, J., et al. (2019). Ionospheric ambipolar electric fields of Mars and Venus: Comparisons between theoretical predictions and direct observations of the electric potential drop. *Geophysical Research Letters*, *46*(3), 1168–1176. https://doi.org/10.1029/2018GL080597

Collinson, G., Mitchell, D., Glocer, A., Grebowsky, J., Peterson, W. K., Connerney, J., et al. (2015). Electric Mars: The first direct measurement of an upper limit for the Martian "Polar Wind" electric potential. *Geophysical Research Letters*, *42*(21), 9128–9134. https://doi.org/10.1002/2015GL065084

Connerney, J. E. P. (2024). *MAVEN MAG calibrated data bundle*. NASA Planetary Data System. https://doi.org/10.17189/1414178

Connerney, J. E. P., Acuña, M. H., Ness, N. F., Kletetschka, G., Mitchell, D. L., Lin, R. P., & Reme, H. (2005). Tectonic implications of Mars crustal magnetism. *Proceedings of the National Academy of Sciences*, *102*(42), 14970–14975. https://doi.org/10.1073/pnas.0507469102

Connerney, J. E. P., Espley, J., Lawton, P., Murphy, S., Odom, J., Oliversen, R., & Sheppard, D. (2015). The MAVEN magnetic field investigation. *Space Science Reviews*, *195*(1–4), 257–291. https://doi.org/10.1007/s11214-015-0169-4

Cowley, S. W. H. (1976). Comments on the merging of nonantiparallel magnetic fields. *Journal of Geophysical Research*, *81*(19), 3455–3458. https://doi.org/10.1029/JA081i019p03455

Cui, J., Wu, X. S., Gu, H., Jiang, F. Y., & Wei, Y. (2019). Photochemical escape of atomic C and N on Mars: Clues from a multi-instrument MAVEN dataset. *Astronomy and Astrophysics*, *621*, A23. https://doi.org/10.1051/0004-6361/201833749

Cui, J., Yelle, R. V., Zhao, L. L., Stone, S., Jiang, F. Y., Cao, Y. T., et al. (2018). The impact of crustal magnetic fields on the thermal structure of the Martian upper atmosphere. *Astrophysical Journal Letters*, *853*(L33), L33. https://doi.org/10.3847/2041-8213/aaa89a

Curry, S. M., Hara, T., Luhmann, J. G., Leblanc, F., Jolitz, R., Mitchell, D., et al. (2025). First direct observations of atmospheric sputtering at Mars. *Science Advances*, *11*(22), eadt1538. https://doi.org/10.1126/sciadv.adt1538

Deca, J., Divin, A., Wang, X., Lembège, B., Markidis, S., Horányi, M., & Lapenta, G. (2016). Three-dimensional full-kinetic simulation of the solar wind interaction with a vertical dipolar lunar magnetic anomaly. *Geophysical Research Letters*, *43*(9), 4136–4144. https://doi.org/10.1002/2016GL068535

Dong, C., Lee, Y., Ma, Y., Lingam, M., Bougher, S., Luhmann, J., et al. (2018). Modeling Martian atmospheric losses over time: Implications for exoplanetary climate evolution and habitability. *Astrophysical Journal Letters*, *859*(L14), L14. https://doi.org/10.3847/2041-8213/aac489

Dong, Y., Brain, D. A., Jarvinen, R., & Poppe, A. R. (2024). Localized hybrid simulation of Martian crustal magnetic cusp regions: Vertical electric potential drop and plasma dynamics. *Journal of Geophysical Research: Space Physics*, *129*(2), e2023JA032050. https://doi.org/10.1029/2023JA032050

Dong, Y., Fang, X., Brain, D. A., McFadden, J. P., Halekas, J. S., Connerney, J. E., et al. (2015). Strong plume fluxes at Mars observed by MAVEN: An important planetary ion escape channel. *Geophysical Research Letters*, *42*(21), 8942–8950. https://doi.org/10.1002/2015GL065346

Du, A., Ge, Y., Wang, H., Li, H., Zhang, Y., Luo, H., et al. (2023). Ground magnetic survey on Mars from the Zhurong rover. *Nature Astronomy*, *7*(9), 1037–1047. https://doi.org/10.1038/s41550-023-02008-7

Dubinin, E., Fraenz, M., Pätzold, M., McFadden, J., Mahaffy, P. R., Eparvier, F., et al. (2017). Effects of solar irradiance on the upper ionosphere and oxygen ion escape at Mars: MAVEN observations. *Journal of Geophysical Research: Space Physics*, *122*(7), 7142–7152. https://doi.org/10.1002/2017JA024126

Dubinin, E., Fraenz, M., Pätzold, M., Woch, J., McFadden, J., Fan, K., et al. (2020). Impact of Martian crustal magnetic field on the ion escape. *Journal of Geophysical Research: Space Physics*, *125*(10), e28010. https://doi.org/10.1029/2020JA028010

Dubinin, E., Lundin, R., Norberg, O., & Pissarenko, N. (1993). Ion acceleration in the Martian tail: Phobos observations. *Journal of Geophysical Research*, *98*(A3), 3991–3997. https://doi.org/10.1029/92JA02233

Dunn, P. A. (2024). *MAVEN insitu key parameters data collection*. NASA Planetary Data System. https://doi.org/10.17189/6jmv-t325

Edberg, N. J. T., Lester, M., Cowley, S. W. H., & Eriksson, A. I. (2008). Statistical analysis of the location of the Martian magnetic pileup boundary and bow shock and the influence of crustal magnetic fields. *Journal of Geophysical Research*, *113*(A8), 2008JA013096. https://doi.org/10.1029/2008JA013096

Egan, H., Jarvinen, R., Ma, Y., & Brain, D. (2019). Planetary magnetic field control of ion escape from weakly magnetized planets. *Monthly Notices of the Royal Astronomical Society*, *488*(2), 2108–2120. https://doi.org/10.1093/mnras/stz1819

Ergun, R. E., Andersson, L., Peterson, W. K., Brain, D., Delory, G. T., Mitchell, D. L., et al. (2006). Role of plasma waves in Mars' atmospheric loss. *Geophysical Research Letters*, *33*(14), 2006GL025785. https://doi.org/10.1029/2006GL025785

Ergun, R. E., Andersson, L. A., Fowler, C. M., Woodson, A. K., Weber, T. D., Delory, G. T., et al. (2016). Enhanced O_2^+ loss at Mars due to an ambipolar electric field from electron heating. *Journal of Geophysical Research: Space Physics*, *121*(5), 4668–4678. https://doi.org/10.1002/2016JA022349

Espley, J. R., Cloutier, P. A., Brain, D. A., Crider, D. H., & Acuña, M. H. (2004). Observations of low-frequency magnetic oscillations in the Martian magnetosheath, magnetic pileup region, and tail. *Journal of Geophysical Research*, *109*(A7), 2003JA010193. https://doi.org/10.1029/2003JA010193

Fan, K., Fraenz, M., Wei, Y., Cui, J., Rong, Z., Chai, L., & Dubinin, E. (2020). Deflection of global ion flow by the Martian crustal magnetic fields. *Astrophysical Journal Letters*, *898*(2), L54. https://doi.org/10.3847/2041-8213/aba519

Fowler, C. M., Andersson, L., Peterson, W. K., Halekas, J., Nagy, A. F., Ergun, R. E., et al. (2018). Correlations between enhanced electron temperatures and electric field wave power in the Martian ionosphere. *Geophysical Research Letters*, *45*(2), 493–501. https://doi.org/10.1002/2017GL073387

Fowler, C. M., McFadden, J., Hanley, K. G., Mitchell, D. L., Curry, S., & Jakosky, B. (2022). In-situ measurements of ion density in the martian ionosphere: Underlying structure and variability observed by the MAVEN-STATIC instrument. *Journal of Geophysical Research: Space Physics*, *127*(8), e2022JA030352. https://doi.org/10.1029/2022JA030352

Fox, J. L., & Hać, A. B. (2018). Escape of $O(^3P)$, $O(^1D)$, and $O(^1S)$ from the Martian atmosphere. *Icarus*, *300*, 411–439. https://doi.org/10.1016/j.icarus.2017.08.041

Frahm, R., Winningham, J., Sharber, J., Scherrer, J., Jeffers, S., Coates, A., et al. (2006). Carbon dioxide photoelectron energy peaks at Mars. *Icarus*, *182*(2), 371–382. https://doi.org/10.1016/j.icarus.2006.01.014

Fuselier, S. A., Petrinec, S. M., Trattner, K. J., Broll, J. M., Burch, J. L., Giles, B. L., et al. (2018). Observational evidence of large-scale multiple reconnection at the Earth's dayside magnetopause. *Journal of Geophysical Research: Space Physics*, *123*(10), 8407–8421. https://doi.org/10.1029/2018JA025681

Futaana, Y., Barabash, S., Wieser, M., Lue, C., Wurz, P., Vorburger, A., et al. (2013). Remote energetic neutral atom imaging of electric potential over a lunar magnetic anomaly. *Geophysical Research Letters*, *40*(2), 262–266. https://doi.org/10.1002/grl.50135

Gao, J. W., Rong, Z. J., Klinger, L., Li, X. Z., Liu, D., & Wei, Y. (2021). A spherical harmonic Martian crustal magnetic field model combining data sets of MAVEN and MGS. *Earth and Space Science*, *8*(10), e01860. https://doi.org/10.1029/2021EA001860

Gronoff, G., Arras, P., Baraka, S., Bell, J. M., Cessateur, G., Cohen, O., et al. (2020). Atmospheric escape processes and planetary atmospheric evolution. *Journal of Geophysical Research: Space Physics*, *125*(8), e27639. https://doi.org/10.1029/2019JA027639

Gronoff, G., Rahmati, A., Wedlund, C. S., Mertens, C. J., Cravens, T. E., & Kallio, E. (2014). The precipitation of keV energetic oxygen ions at Mars and their effects during the comet siding spring approach. *Geophysical Research Letters*, *41*(14), 4844–4850. https://doi.org/10.1002/2014GL060902

Gu, H., Cui, J., Niu, D., He, Z., & Li, K. (2020). Monte Carlo calculations of helium escape on Mars via energy transfer from hot oxygen atoms. *Astrophysical Journal*, *902*(2), 121. https://doi.org/10.3847/1538-4357/abb6e9

Halekas, J., Saito, Y., Delory, G., & Farrell, W. (2011). New views of the lunar plasma environment. *Planetary and Space Science*, *59*(14), 1681–1694. https://doi.org/10.1016/j.pss.2010.08.011

Halekas, J. S. (2024). *MAVEN SWIA calibrated data bundle*. NASA Planetary Data System. https://doi.org/10.17189/1414182

Halekas, J. S., Taylor, E. R., Dalton, G., Johnson, G., Curtis, D. W., McFadden, J. P., et al. (2015). The solar wind ion analyzer for MAVEN. *Space Science Reviews*, *195*(1–4), 125–151. https://doi.org/10.1007/s11214-013-0029-z

Hanley, K. G., Fowler, C. M., McFadden, J. P., Mitchell, D. L., & Curry, S. (2022). MAVEN-STATIC observations of ion temperature and initial ion acceleration in the Martian ionosphere. *Geophysical Research Letters*, *49*(18), e2022GL100182. https://doi.org/10.1029/2022GL100182

Harada, Y., Halekas, J. S., DiBraccio, G. A., Xu, S., Espley, J., Mcfadden, J. P., et al. (2018). Magnetic reconnection on dayside crustal magnetic fields at Mars: MAVEN observations. *Geophysical Research Letters*, *45*(10), 4550–4558. https://doi.org/10.1002/2018GL077281

Harada, Y., Mitchell, D. L., Halekas, J. S., McFadden, J. P., Mazelle, C., Connerney, J. E. P., et al. (2016). MAVEN observations of energy-time dispersed electron signatures in Martian crustal magnetic fields. *Geophysical Research Letters*, *43*(3), 939–944. https://doi.org/10.1002/2015GL067040

Harnett, E. M., & Winglee, R. M. (2005). Three-dimensional fluid simulations of plasma asymmetries in the Martian magnetotail caused by the magnetic anomalies. *Journal of Geophysical Research*, *110*(A7), 2003JA010315. https://doi.org/10.1029/2003JA010315

Jakosky, B. M., Grebowsky, J. M., Luhmann, J. G., Connerney, J., Eparvier, F., Ergun, R., et al. (2015). MAVEN observations of the response of Mars to an interplanetary coronal mass ejection. *Science*, *350*(6261), aad0210. https://doi.org/10.1126/science.aad0210

Jakosky, B. M., Lin, R. P., Grebowsky, J. M., Luhmann, J. G., Mitchell, D. F., Beutelschies, G., et al. (2015). The Mars Atmosphere and Volatile Evolution (MAVEN) mission. *Space Science Reviews*, *195*(1–4), 3–48. https://doi.org/10.1007/s11214-015-0139-x

Jakosky, B. M., & Phillips, R. J. (2001). Mars' volatile and climate history. *Nature*, *412*(6843), 237–244. https://doi.org/10.1038/35084184

Jeans, J. (2009). *The dynamical theory of gases* (4th ed.). Cambridge University Press. https://doi.org/10.1017/CBO9780511694370

Krymskii, A. M., Breus, T. K., Ness, N. F., Acuña, M. H., Connerney, J. E. P., Crider, D. H., et al. (2002). Structure of the magnetic field fluxes connected with crustal magnetization and topside ionosphere at Mars. *Journal of Geophysical Research*, *107*(A9). https://doi.org/10.1029/2001JA000239

Lammer, H., Bredehöft, J. H., Coustenis, A., Khodachenko, M. L., Kaltenegger, L., Grasset, O., et al. (2009). What makes a planet habitable? *Astronomy and Astrophysics Review*, *17*, 181–249. https://doi.org/10.1007/s00159-009-0019-z

Lue, C., Futaana, Y., Barabash, S., Wieser, M., Holmström, M., Bhardwaj, A., et al. (2011). Strong influence of lunar crustal fields on the solar wind flow: Influence of lunar crustal fields. *Geophysical Research Letters*, *38*(3). https://doi.org/10.1029/2010GL046215

Luhmann, J. G., Johnson, R. E., & Zhang, M. H. G. (1992). Evolutionary impact of sputtering of the Martian atmosphere by O^+ pickup ions. *Geophysical Research Letters*, *19*(21), 2151–2154. https://doi.org/10.1029/92GL02485

Luhmann, J. G., & Kozyra, J. U. (1991). Dayside pickup oxygen ion precipitation at Venus and Mars: Spatial distributions, energy deposition and consequences. *Journal of Geophysical Research*, *96*(A4), 5457–5467. https://doi.org/10.1029/90JA01753

Luhmann, J. G., & Schwingenschuh, K. (1990). A model of the energetic ion environment of Mars. *Journal of Geophysical Research*, *95*(A2), 939–945. https://doi.org/10.1029/JA095iA02p00939

Lundin, R., Barabash, S., Andersson, H., Holmström, M., Grigoriev, A., Yamauchi, M., et al. (2004). Solar wind-induced atmospheric erosion at Mars: First results from ASPERA-3 on Mars Express. *Science*, *305*(5692), 1933–1936. https://doi.org/10.1126/science.1101860

Lundin, R., Barabash, S., Yamauchi, M., Nilsson, H., & Brain, D. (2011). On the relation between plasma escape and the Martian crustal magnetic field: Plasma escape and Martian magnetic field. *Geophysical Research Letters*, *38*(2), n/a-n–a. https://doi.org/10.1029/2010GL046019

Lundin, R., & Dubinin, E. M. (1992). Phobos-2 results on the ionospheric plasma escape from Mars. *Advances in Space Research*, *12*(9), 255–263. https://doi.org/10.1016/0273-1177(92)90338-X

Lundin, R., Lammer, H., & Ribas, I. (2007). Planetary magnetic fields and solar forcing: Implications for atmospheric evolution. *Space Science Reviews*, *129*(1–3), 245–278. https://doi.org/10.1007/s11214-007-9176-4

Lundin, R., Winningham, D., Barabash, S., Frahm, R., Holmström, M., Sauvaud, J.-A., et al. (2006). Plasma acceleration above Martian magnetic anomalies. *Science*, *311*(5763), 980–983. https://doi.org/10.1126/science.1122071

Ma, Y., Nagy, A. F., Hansen, K. C., DeZeeuw, D. L., Gombosi, T. I., & Powell, K. G. (2002). Three-dimensional multispecies MHD studies of the solar wind interaction with Mars in the presence of crustal fields. *Journal of Geophysical Research*, *107*(A10). https://doi.org/10.1029/2002JA009293

Ma, Y., Nagy, A. F., Sokolov, I. V., & Hansen, K. C. (2004). Three-dimensional, multispecies, high spatial resolution MHD studies of the solar wind interaction with Mars. *Journal of Geophysical Research*, *109*(A7), 2003JA010367. https://doi.org/10.1029/2003JA010367

Ma, Y.-J., & Nagy, A. F. (2007). Ion escape fluxes from Mars. *Geophysical Research Letters*, *34*(8), 2006GL029208. https://doi.org/10.1029/2006GL029208

Madanian, H., Hesse, T., Duru, F., Pilinski, M., & Frahm, R. (2024). Ionospheric density depletions around crustal fields at Mars and their connection to ion frictional heating. *Annales Geophysicae*, *42*(1), 69–78. https://doi.org/10.5194/angeo-42-69-2024

Mantas, G. P., & Hanson, W. B. (1979). Photoelectron fluxes in the Martian ionosphere. *Journal of Geophysical Research*, *84*(A2), 369–386. https://doi.org/10.1029/JA084iA02p00369

McFadden, J. P. (2024). *MAVEN STATIC calibrated data bundle*. NASA Planetary Data System. https://doi.org/10.17189/1414180

McFadden, J. P., Kortmann, O., Curtis, D., Dalton, G., Johnson, G., Abiad, R., et al. (2015). MAVEN SupraThermal and Thermal Ion Compostion (STATIC) instrument. *Space Science Reviews*, *195*(1–4), 199–256. https://doi.org/10.1007/s11214-015-0175-6

Mitchell, D. L. (2023). *MAVEN SWEA calibrated data bundle*. NASA Planetary Data System. https://doi.org/10.17189/1414181

Mitchell, D. L., Mazelle, C., Sauvaud, J.-A., Thocaven, J.-J., Rouzaud, J., Fedorov, A., et al. (2016). The MAVEN solar wind electron analyzer. *Space Science Reviews*, *200*(1–4), 495–528. https://doi.org/10.1007/s11214-015-0232-1

Moore, T. E., Fok, M.-C., & Chandler, M. O. (2002). The dayside reconnection X line. *Journal of Geophysical Research*, *107*(A10). SMP 26-1. https://doi.org/10.1029/2002JA009381

Nilsson, H., Edberg, N. J., Stenberg, G., Barabash, S., Holmström, M., Futaana, Y., et al. (2011). Heavy ion escape from Mars, influence from solar wind conditions and crustal magnetic fields. *Icarus*, *215*(2), 475–484. https://doi.org/10.1016/j.icarus.2011.08.003

Otsuka, Y., Shinbori, A., Sori, T., Tsugawa, T., Nishioka, M., & Huba, J. D. (2021). Plasma depletions lasting into daytime during the recovery phase of a geomagnetic storm in May 2017: Analysis and simulation of GPS total electron content observations. *Earth and Planetary Physics*, *5*(5), 427–434. https://doi.org/10.26464/epp2021046

Otsuka, Y., Shiokawa, K., Ogawa, T., & Wilkinson, P. (2002). Geomagnetic conjugate observations of equatorial airglow depletions. *Geophysical Research Letters*, *29*(15), 43-1–43-4. https://doi.org/10.1029/2002GL015347

Owen, J. E. (2019). Atmospheric escape and the evolution of Close-In exoplanets. *Annual Review of Earth and Planetary Sciences*, *47*(1), 67–90. https://doi.org/10.1146/annurev-earth-053018-060246

Oya, H., Takahashi, T., & Watanabe, S. (1986). Observation of low latitude ionosphere by the impedance probe on board the hinotori satellite. *Journal of Geomagnetism and Geoelectricity*, *38*(2), 111–123. https://doi.org/10.5636/jgg.38.111

Pérez-de Tejada, H. (1987). Plasma flow in the Mars magnetosphere. *Journal of Geophysical Research*, *92*(A5), 4713–4718. https://doi.org/10.1029/JA092iA05p04713

Pérez-de-Tejada, H. (1998). Momentum transport in the solar wind erosion of the Mars ionosphere. *Journal of Geophysical Research*, *103*(E13), 31499–31508. https://doi.org/10.1029/1998JE900001

Poppe, A. R., Brain, D. A., Dong, Y., Xu, S., & Jarvinen, R. (2021). Particle-In-cell modeling of Martian magnetic cusps and their role in enhancing nightside ionospheric ion escape. *Geophysical Research Letters*, *48*(1), e2020GL090763. https://doi.org/10.1029/2020GL090763

Poppe, A. R., Halekas, J. S., Delory, G. T., & Farrell, W. M. (2012). Particle-in-cell simulations of the solar wind interaction with lunar crustal magnetic anomalies: Magnetic cusp regions. *Journal of Geophysical Research*, *117*(A9), 2012JA017844. https://doi.org/10.1029/2012JA017844

Ramstad, R., Barabash, S., Futaana, Y., Nilsson, H., & Holmström, M. (2016). Effects of the crustal magnetic fields on the Martian atmospheric ion escape rate. *Geophysical Research Letters*, *43*(20). https://doi.org/10.1002/2016GL070135

Saito, Y., Nishino, M. N., Fujimoto, M., Yamamoto, T., Yokota, S., Tsunakawa, H., et al. (2012). Simultaneous observation of the electron acceleration and ion deceleration over lunar magnetic anomalies. *Earth Planets and Space*, *64*(2), 83–92. https://doi.org/10.5047/eps.2011.07.011

Su, Z., Liu, N., Gao, Z., Wang, B., Zheng, H., Wang, Y., & Wang, S. (2020). Rapid Landau heating of Martian topside ionospheric electrons by large-amplitude magnetosonic waves. *Geophysical Research Letters*, *47*(20), e2020GL090190. https://doi.org/10.1029/2020GL090190

Tian, F. (2015). Atmospheric escape from solar system terrestrial planets and exoplanets. *Annual Review of Earth and Planetary Sciences*, *43*(1), 459–476. https://doi.org/10.1146/annurev-earth-060313-054834

Trattner, K. J., Petrinec, S. M., & Fuselier, S. A. (2021). The location of magnetic reconnection at Earth's magnetopause. *Space Science Reviews*, *217*(3), 41. https://doi.org/10.1007/s11214-021-00817-8

Wang, J., Yu, J., Xu, X., Cui, J., Cao, J., Ye, Y., et al. (2021). MAVEN observations of magnetic reconnection at Martian induced magnetopause. *Geophysical Research Letters*, *48*(21), e2021GL095426. https://doi.org/10.1029/2021GL095426

Wang, M., Guan, Z., Xie, L., Lu, J., Wei, G., Sui, H., et al. (2024). The effect of the interplanetary magnetic field clock angle and the latitude location of the intense crustal magnetic field on the ion escape at Mars: An MHD simulation study. *Journal of Geophysical Research: Space Physics*, *129*(8), e2024JA032806. https://doi.org/10.1029/2024JA032806

Weber, T., Brain, D., Xu, S., Mitchell, D., Espley, J., Mazelle, C., et al. (2021). Martian crustal field influence on O^+ and O_2^+ escape as measured by MAVEN. *Journal of Geophysical Research: Space Physics*, *126*(8), e2021JA029234. https://doi.org/10.1029/2021JA029234

Wei, Y., Fraenz, M., Dubinin, E., Woch, J., Lühr, H., Wan, W., et al. (2012). Enhanced atmospheric oxygen outflow on Earth and Mars driven by a corotating interaction region. *Journal of Geophysical Research*, *117*(A3), 2011JA017340. https://doi.org/10.1029/2011JA017340

Xu, S., Mitchell, D., Liemohn, M., Fang, X., Ma, Y., Luhmann, J., et al. (2017). Martian low-altitude magnetic topology deduced from MAVEN/SWEA observations. *Journal of Geophysical Research: Space Physics*, *122*(2), 1831–1852. https://doi.org/10.1002/2016JA023467

Xu, S., Mitchell, D. L., McFadden, J. P., Collinson, G., Harada, Y., Lillis, R., et al. (2018). Field-aligned potentials at Mars from MAVEN observations. *Geophysical Research Letters*, *45*(19). https://doi.org/10.1029/2018GL080136

Ye, Y., Xu, X., Lee, L.-C., Yu, J., Wang, J., Zhu, B., et al. (2024). In situ observation of mass ejections caused by magnetic reconnections in the ionosphere of Mars. *Nature Astronomy*, *8*(7), 838–845. https://doi.org/10.1038/s41550-024-02254-3

Zhang, C., Nilsson, H., Ebihara, Y., Yamauchi, M., Persson, M., Rong, Z., et al. (2023). Detection of magnetospheric ion drift patterns at Mars. *Nature Communications*, *14*(1), 6866. https://doi.org/10.1038/s41467-023-42630-7

Zhang, C., Rong, Z., Nilsson, H., Klinger, L., Xu, S., Futaana, Y., et al. (2021). MAVEN observations of periodic low-altitude plasma clouds at Mars. *Astrophysical Journal Letters*, *922*(2), L33. https://doi.org/10.3847/2041-8213/ac3a7d

Zhang, C., Zhou, H., Dong, C., Harada, Y., Yamauchi, M., Xu, S., et al. (2024). Source of drift-dispersed electrons in Martian crustal magnetic fields. *The Astrophysical Journal*, *972*(2), 153. https://doi.org/10.3847/1538-4357/ad64d5

Zhang, H., Fu, S., Fu, S., Zhong, J., Ni, B., Wei, Y., et al. (2022). A highway for atmospheric ion escape from Earth during the impact of an interplanetary coronal mass ejection. *Astrophysical Journal*, *937*(1), 4. https://doi.org/10.3847/1538-4357/ac8a93

Zhang, H., Zhong, J., Fu, S., Pu, Z., Wei, Y., Xie, L., et al. (2023). Large-scale inverted-V channels of upflowing oxygen ions pumped by Alfvén waves. *Earth and Planetary Physics*, *7*(6), 640–654. https://doi.org/10.26464/epp2023082